remote sensing

MDPI

Article

Development of Geo-KOMPSAT-2A Algorithm for Sea-Ice Detection Using Himawari-8/AHI Data

Donghyun Jin [1], Sung-Rae Chung [2], Kyeong-Sang Lee [1], Minji Seo [1], Sungwon Choi [1], Noh-Hun Seong [1], Daeseong Jung [1], Suyoung Sim [1], Jinsoo Kim [1] and Kyung-Soo Han [1,*]

[1] Division of Earth Environmental System Science (Major of Spatial Information System Engineering), Pukyong National University, 45, Yongso-ro, Nam-gu, Busan 48513, Korea; dhyun201@pukyong.ac.kr (D.J.); kyeongsang@pukyong.ac.kr (K.-S.L.); seo_mj@pukyong.ac.kr (M.S.); cswyj94@pukyong.ac.kr (S.C.); seongnohhun@pukyong.ac.kr (N.-H.S.); jungdaeseong@pukyong.ac.kr (D.J.); simsuyoung@pukyong.ac.kr (S.S.); jinsookim@pknu.ac.kr (J.K.)

[2] National Meteorological Satellite Center, 64-18, Guam-gil, Gwanghyewon-myeon, Jincheon-gun, Chungcheongbuk-do 27803, Korea; csr@korea.kr

* Correspondence: Kyung-soo.han@pknu.ac.kr; Tel.: +82-51-629-6659

Received: 3 June 2020; Accepted: 12 July 2020; Published: 14 July 2020

Abstract: Sea ice is an important meteorological factor affecting the global climate system, but it is difficult to observe in sea ice ground truth data because of its location mainly at high latitudes and in polar regions. Accordingly, sea-ice detection research has been actively conducted using satellites, since the 1970s. Polar-orbiting and geostationary satellites are used for this purpose; notably, geostationary satellites are capable of real-time monitoring of specific regions. In this paper, we introduce the Geo-KOMPSAT-2A (GK-2A)/Advanced Meteorological Imager (AMI) sea-ice detection algorithm using Japan Meteorological Agency (JMA) Himawari-8/Advanced Himawari Imager (AHI) data as proxy data. The GK-2A/AMI, which is Korea Meteorological Administration (KMA)'s next-generation geostationary satellite launched in December 2018 and Himawari-8/AHI have optically similar channel data, and the observation area includes East Asia and the Western Pacific. The GK-2A/AMI sea-ice detection algorithm produces sea-ice data with a 10-min temporal resolution, a 2-km spatial resolution and sets the Okhotsk Sea and Bohai Sea, where the sea ice is distributed during the winter in the northern hemisphere. It used National Meteorological Satellite Center (NMSC) cloud mask as the preceding data and a dynamic threshold method instead of the static threshold method that is commonly performed in existing sea-ice detection studies. The dynamic threshold methods for sea-ice detection are dynamic wavelength warping (DWW) and IST_0 method. The DWW is a method for determining the similarity by comparing the pattern of reflectance change according to the wavelength of two satellite data. The IST_0 method detects sea ice by using the correlation between 11.2-µm brightness temperature ($BT_{11.2}$) and brightness temperature difference (BTD) [$BT_{11.2}$–$BT_{12.3}$] according to ice surface temperature (IST). In addition, the GK-2A/AMI sea-ice detection algorithm reclassified the cloud area into sea ice using a simple test. A comparison of the sea-ice data derived the GK-2A/AMI sea-ice detection algorithm with the S-NPP/visible infrared imaging radiometer suite (VIIRS) sea ice characterization product indicates consistency of 99.0% and inconsistency of 0.9%. The overall accuracy (OA) of GK-2A/AMI sea-ice data with the sea ice region of interest (ROI) data, which is constructed by photo-interpretation method from RGB images, is 97.2%.

Keywords: geostationary satellites; GK-2A AMI; Himawari-8 AHI; sea-ice detection algorithm; the sea of Okhotsk

1. Introduction

Areas covered by sea ice have a higher reflectance of incident solar energy, compared to ice-free sea water. This affects the surface energy balance [1] and is one of the factors that influences the global climate system. Information on the presence and distribution of sea ice has been used for long-term climate research. In addition, information on sea ice is employed not only for long-term climate studies, but also for short-term forecasting models such as weather forecasting and also needed for ship navigation. The distribution of sea ice is highly dependent on the season; the largest monthly amount of Northern Hemisphere sea ice occurs in March, while the smallest amount occurs in September [2]. sea ice is mainly distributed in polar or high-latitude regions, where it is difficult to perform in situ observations. Therefore, satellite data are generally utilized to detect sea ice for polar or high-latitude regions. The satellite measurements for mapping sea ice have been performed since the 1970s, using optical and microwave instruments. Satellite-based microwave measurements can detect sea ice below the clouds and night–time. However, this spatial resolution of microwave based sea ice data are approximately 6.25 km (AMSR-2 sea ice products) [3]. Although microwave-based sea-ice data such as AMSR-2 sea ice products have a spatial resolution of more than five kilometers, AMSR-2 sea ice products can cover all polar regions within a day. Sentinel-1A and 1B's synthetic aperture radar (SAR)-based sea ice material can also cover most of the polar regions in one day. Sea-ice data derived from optical instruments onboard of polar-orbiting and geostationary satellites cannot detect surface properties under cloud conditions and night–time. However, the spatial resolution (500 m -2 km) of the optical instruments [4–7] is higher than that for microwave satellite data except for SAR-based sea-ice data [8]. Microwave-based satellites may produce SAR with a resolution of 100 m. The SAR-based sea-ice data provides sea ice information in smaller oceans, like Baltic Sea, in local areas in general and ice charting for ship navigation [9]. In the case of optical satellites, there are restrictions on various environmental conditions, but a geostationary satellite among optical satellites can observe a region of interest with a high temporal resolution.

To date, many institutions are performing sea-ice detection using optical satellites (e.g., polar-orbiting satellites, such as the National Aeronautics and Space Administration (NASA) Terra/moderate resolution imaging spectroradiometer (MODIS) [4] and Suomi National Polar-orbiting Partnership (S-NPP) visible infrared imaging radiometer suite (VIIRS) [5] and geostationary satellites, such as the NASA geostationary operational environmental satellite (GOES)-R (same as GOES-16) advanced baseline imager (ABI) [6] and the Japan Meteorological Agency (JMA) Himawari-8/advanced Himawari imager (AHI) [7], which is equipped with optical sensors). The GOES-R/ABI calculates sea-ice data every 180 min based on a full disk (whole-earth images), and spatial resolution is provided at two kilometers and typical target areas are Great Lakes. The products are scheduled to become operational for GOES-R in 2020. Himawri-8/AHI-based sea ice data are calculated every 10 min on a full disk basis, spatial resolution is provided at two kilometers and the typical target oceans are the Okhotsk Sea and the max viewing zenith angle for usable sea ice data are up to 65.0°. Polar-orbiting satellite-based sea-ice data have higher spatial resolution than geostationary satellite-based sea-ice data and can utilize this feature to identify the development and ice flow distribution. The polar-orbiting satellite can observe whole polar area, but geostationary satellites only up to like 70° N. geostationary satellite-based sea-ice data have a lower spatial resolution than polar-orbiting satellite-based sea-ice data, but have much higher observation temporal frequency (e.g., geostationary satellite: 10 min, Polar-orbiting satellite: one to two times per day except for the high arctic area). The advantage of high frequency of observation is that the chance to observe clear-sky is high [10]. In addition, since full disk can be observed in a short time, real-time monitoring is possible for the sea ice area. This is particularly useful when monitoring hazardous and highly mobile weather features. Thus, the use of geostationary satellites is essential for sea-ice detection. These data can be applied to reduce the potential false positive rates of polar-orbiting satellite-based daily sea-ice data. The geostationary satellite-based sea-ice detection produces more sea-ice data than polar-orbiting satellites in 24 h; this compensates for lack for the sea ice time series when calculating daily data. For example, when the daily composite is performed at a time during sea ice melting season, the distribution of sea ice may change even in one day. Since polar-orbiting satellite-based sea-ice data can be observed two times per day during daily composite, the gap between two observations is large at time intervals. This may affect the quality of sea-ice data when performing an one day composite [11]. The Korea Meteorological Administration (KMA) has been conducting sea-ice detection since 2010 using the geostationary Communications, Ocean and Meteorological Satellite (COMS)/Meteorological Imager (MI). However, COMS/MI operations ended in March 2020. For this reason, KMA developed the next-generation weather satellite Geo-KOMPSAT-2A (GK-2A), which was launched in December 2018. It has an Advanced Meteorological Imager (AMI) onboard with 16 channels in the visible (VIS) and infrared (IR) bands of the electromagnetic spectrum (11 more channels, compared to the COMS/MI) and is located over the equator at a longitude of 128.2° E. It provides full disk images at 10-min intervals and has a higher temporal and spatial resolution, compared to the COMS/MI. There has recently been active research concerning the development of meteorological products was conducted that utilize the GK-2A/AMI [12–17]. We used AHI data as a proxy for the development of GK-2A/AMI sea-ice detection algorithm. The AHI is a multispectral imaging device with up to 16 channels of data [7,18], with specifications similar to those of the GK-2A/AMI. It is mounted on the JMA Himawari-8 geostationary meteorological satellite, which was launched in October 2014. The AHI has similar spectral and optical characteristics to the GK-2A/AMI; one characteristic constitutes the temporal resolution of 10 min for a full disk image. The AMI has 16 channels: three visible, two near-infrared (NIR), two short-wave infrared (SWIR) and nine IR. This similarity enabled use of AHI data as proxy data. Although the GK-2A/AMI was launched in December 2018, the actual GK-2A/AMI channel data were produced from June 2019 because the in-orbit test (IOT) process for the GK-2A/AMI channel data must be performed in advance. In the future, the GK-2A/AMI sea-ice detection algorithm will be optimized by securing additional GK-2A/AMI data for 2019–2020 winter season. Similar to snow, sea ice has high reflectance at visible wavelengths and low reflectance at short-wave infrared wavelengths. Most optical sensors, including the geostationary satellites, employ a static threshold method that utilizes the unique optical properties of sea ice to perform detection. The MODIS/Terra, S-NPP/VIIRS and GOES-R/ABI of NASA mainly utilize the channel reflectance, normalized difference snow index (*NDSI*, Equation (1)) and ice surface temperature (IST) [4,6,19].

$$NDSI = \frac{(R_{0.64} - R_{1.61})}{(R_{0.64} + R_{1.61})}. \tag{1}$$

NDSI is normalized difference of two bands (one in the visible and one in the short-wave infrared parts of spectrum). However, reflectance varies depending on sea ice roughness, thickness, salinity and solar zenith angle (SZA) [20–22]. For this reason, Nazari and Khanbilvardi (2011) [23] performed the sea-ice detection by applying the dynamic threshold method considering the reflectance of sea ice. In addition, sea ice can be divided into ice covered with snow and pure ice without snow. Satellite-based sea-ice detection or research on sea ice considers not only pure ice, but also snow characteristics due to snow-covered ice [20]. When detecting snow cover using satellite data, the spectral reflectance of the snow cover is sensitive to the particle size [24]. For this reason, GOES-R/ABI snow cover algorithm considers the spectral characteristics of the snow according to the particle size of the snow [25]. Xin et al. (2012) [26] conducted a variability analysis of NDSI in snow regions depending on the viewing angle. In this way, the studies on snow and sea ice analyzed the variability of snow and sea ice reflectance, and considering this, the dynamic threshold method according to the conditions of snow and sea ice was applied to detect snow and sea ice. Sea ice, including ice covered with snow, has variability in reflectance, but except for variability in SZA, the pattern of change in reflectance with wavelength does not change. Furthermore, sea-ice detection using satellite data utilizes IST, which is calculated using the method of Key et al. (1997) [27] in addition to reflectance and NDSI. In addition to sea-ice detection using IST, sea-ice detection studies using object-based methods and classification and regression tree methods are also being conducted [28–30]. Sea ice detection using IST with high accuracy can reduce uncertainty. However, in order to use IST for sea-ice detection, empirical coefficients for calculating IST for each satellite must be selected and each coefficient must be calculated in advance through linear regression considering atmospheric effects and humidity conditions. The GK-2A/AMI has no algorithm to calculate IST and Himawari-8/AHI-based IST data have not been produced. Therefore, in GK-2A/AMI sea-ice detection algorithm, the dynamic threshold method using the correlation between 11.2-µm brightness temperature ($BT_{11.2}$) and brightness temperature difference (BTD) [$BT_{11.2}$–$BT_{12.3}$] which is simple and efficient without IST counting process is used for sea-ice detection. In this study, the 0.64-µm reflectance was denoted by $R_{0.64}$ and the 11.2-µm BT was denoted by $BT_{11.2}$.

To develop the next-generation weather satellite GK-2A/AMI sea-ice detection algorithm, we applied dynamic threshold methods to consider the variability of sea ice (e.g., DWW), in which the IST calculation is omitted (e.g., IST_0 method), by using Himawari-8/AHI for proxy data. Among the GK-2A/AMI and Himawari-8/AHI observation areas, oceans with sea ice are the Okhotsk Sea [31–35] and the Bohai Sea [20,36–41]. Various studies related to sea ice have been conducted in these areas. Section 2 describes the data and research areas needed to build and perform the GK-2A/AMI sea-ice detection algorithm. Section 3 presents the GK-2A/AMI sea-ice detection algorithm. Section 4 is about the performance evaluation of the GK-2A/AMI sea-ice detection algorithm and Section 5 is the summary, discussions and conclusion of this study.

2. Materials

2.1. Study Area

Our study region covered the Okhotsk Sea and the Bohai Sea (Figure 1). The Okhotsk Sea, which extends as far south as 45° N, is the southernmost ocean in the North Polar that is covered with sea ice during winter [31]. Minervin et al. (2015) [32] analyzed the Okhotsk Sea for 85 years and studied a stable sea ice area that preserves the characteristics of the sea ice state during various stages of ice development. The sea ice thickness on the Okhotsk Sea has lee than 1 m, and the Okhotsk Sea is typically covered by ice from January to March [33]. In the Okhotsk Sea, it has been suggested that this process plays an important role in the meridian circulation and plays an important role in the climate system of the Okhotsk Sea and the North Pacific region [34,35]. In the Okhotsk Sea, sea ice begins to appear in December and is distributed over 70%–80% of the region. Therefore, this region has been applied in many studies concerning sea ice [7,31,33,34]. The Bohai Sea is located on the north side of the Yellow Sea, and can be separated into Liaodong Bay, Bohai Bay and Laizhou Bay (from north to south). In this bay, the spatial and temporal changes in the amount and thickness of sea ice vary greatly with the fluctuations in winter. The period of sea ice existence is about 55 to 120 days and the thickness of ice is 30–50 cm [20]. Bohai Sea has a smaller thickness than sea ice in other regions, and its distribution is limited, but this sea area is also widely used for research on sea ice (e.g., analysis of long-term sea ice area variability, sea-ice detection using satellite data and monitoring of spatial and temporal distribution of satellite-based sea ice) [20,36–41].

2.2. Satellite Data

We used the Himawari-8/AHI dataset (proxy data) to develop a GK-2A/AMI sea-ice detection algorithm. The AHI on board the geostationary Himawari-8 is the first in a series of next-generation weather imagers and has a center longitude of 140.7°E. The Himawari-8/AHI provides 16 channels data and observes every 10 min based on the full disk. Its spatial resolution of 0.64-µm channel data are 500 m, 0.46 µm, 0.51 µm and 0.86 µm is 1 km and IR channel is 2 km. The fields-of-view of Himawari-8/AHI is ±75.0°. The GK-2A/AMI sea-ice detection algorithm collected Himawari-8/AHI data at 10-min intervals from January to March 2018 for use as proxy data. We employed three visible bands (blue: 0.47 µm; green: 0.51 µm; red: 0.64 µm), one NIR band (0.86 µm), one SWIR band (1.6 µm) for reflectance and three IR bands (3.9 µm, 11.2 µm and 12.4 µm) for BT. The process of calibrating channel data to reflectance and BT is provided by the National Meteorological Satellite

Center (NMSC). Besides satellite channel data, we applied a latitude, longitude, land/sea mask, which were provided by NMSC to distinguish between the land and ocean and a cloud mask for excluding cloudy areas. The cloud mask was produced by the GK-2A/AMI cloud detection algorithm from NMSC, using Himawari-8/AHI data [42]. The GK-2A/AMI cloud mask algorithm applies to the threshold method that utilizes the spectral characteristics of cloud and is currently used in the field by NMSC. The GK-2A/AMI cloud mask was compared with MODIS cloud mask (MYD35), its accuracy is product of detection (POD) of 92%, false alarm ratio (FAR) of 13%. The POD is the ratio of GK-2A/AMI cloud mask classified as cloud among the areas classified by MODIS cloud mask as cloud. The FAR is the ratio of the cloud derived for GK-2A/AMI cloud mask among the pixels not classified by MODIS cloud mask as cloud. Details of the POD, FAR calculation are given in Section 4.1. The GK-2A/AMI cloud mask is currently providing cloud information with three flags, namely, high-confidence cloudy, low-confidence cloudy and high-confidence clear. The Himawri-8/AHI RGB image provided by World Science Data Bank (WSDbank) was employed [43]. WSDbank's RGB image developed a web-based data visualization for Himawari-8 satellite sensed images in real time (10 min) and with full resolution (1 km). WSDbank converts the original graphic file using ImageMagick (ImageMagick Studio LLC 2016) to adjust the brightness of the image.

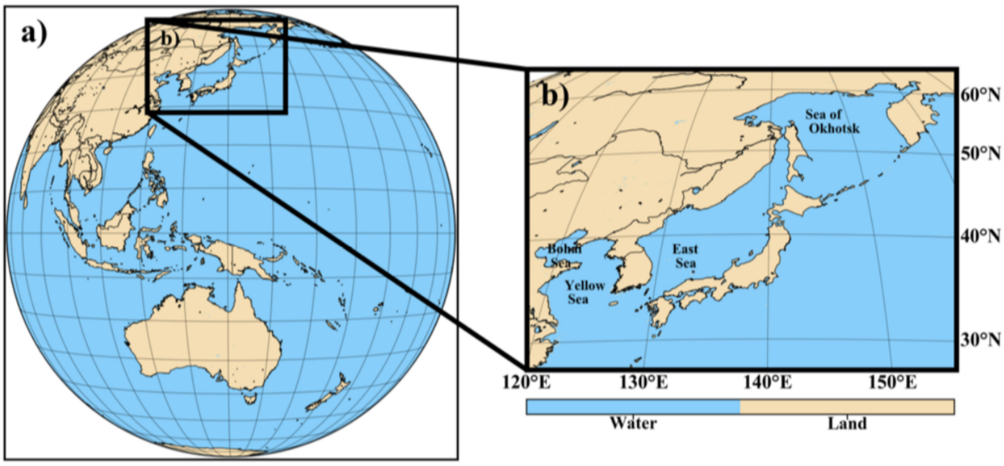

Figure 1. Study area on the GK-2A/AMI sea-ice detection algorithm, (**a**) Himawrai-8/AHI full disk, (**b**) extended study area involving Okhotsk Sea and Bohai Sea.

The Terra/MODIS sea ice extent (MOD29) data, provided by the National snow and ice data center (NSIDC) and NASA, were utilized as reference data for the construction of the GK-2A/AMI sea-ice detection algorithm. The temporal and spatial resolution of the MOD29 data are 5 min and 1 km. The accuracy of sea ice extent data were not quantitatively evaluated; however, qualitative evaluations suggested that the sea ice extent is very accurate under clear-sky conditions [44]. The accuracy of IST data are 1–3 K under ideal conditions (i.e., clear sky and the SZA is less than 85°) [45–47]. The MODIS sea ice extent is applied to various sea ice studies [48,49]. We utilized MODIS sea-ice data from December 2015 to March 2016, corresponding to the Northern Hemisphere winter. The data contained sea ice extent (e.g., the presence or absence of sea ice), IST and quality assessment information. We employed MODIS sea ice extent and IST to set a dynamic threshold for use in sea-ice detection. When utilized as reference data, we applied to good quality sea ice and ocean (ice-free water) pixels from MODIS sea ice extent data.

The Terra/MODIS snow cover (MOD10) product, also provided by NSIDC and NASA, was used as reference data for construction of the snow spectral library for dynamic wavelength warping (DWW). These data have 5-min temporal resolution and 500-m spatial resolution. The overall absolute accuracy of the MODIS snow cover product is approximately 93% [50]. The MODIS snow cover product was validated by several studies [51–53] and is applied for many climate and snow monitoring applications [54]. We employed MODIS snow cover data from December 2015 to March 2016, corresponding to the Northern Hemisphere winter. These data contained snow cover information and quality assessment information. The GK-2A/AMI sea-ice detection algorithm utilized NDSI snow cover data among the MOD10 Dataset. The valid range of NDSI snow cover has distributed in the range of 0–100, but we considered only the pixels with NDSI snow cover over 50 as snow cover. The quality flag data have consisted of 0 = bad, 1 = good, 2 = ok, 3 = poor-not used, 4 = other-not used, 211 = night, 239 = ocean, 255 = unusable L1B data or no data. We only applied to snow cover data with a "good" quality flag. The quality-controlled MODIS snow cover product was employed to build a snow spectral library, which is a reference material for DWW method. Sea ice also exists in snow-covered ice areas and MOD10 data were applied to consider the spectral properties of snow-covered ice areas.

The Northern Hemisphere equal-area scalable earth-grid (EASE-Grid) v2.0 weekly snow cover and sea ice cover product, provided by NSIDC, were used to construct long-term sea-ice data for classifying the sea ice candidate pixels. These data provided information concerning snow cover and sea ice worldwide. The sea ice extent is re-gridded to EASE-grid using sea ice concentrations from the Nimbus-7 scanning multichannel microwave radiometer and the defense meteorological satellite program special sensor microwave imager-special sensor microwave imager/sounder passive microwave data. These data have 1-week temporal resolution and 25-km spatial resolution and were applied in various studies, as well as in studies monitoring snow and sea ice [55,56]. We utilized the Northern Hemisphere EASE-Grid v2.0 weekly snow cover and sea ice cover product from 1980 to 2014; we only applied to sea ice and ice-free water from the data flag information.

The S-NPP/VIIRS sea ice characterization (SIC) environmental data record (EDR) product was applied to evaluate the GK-2A/AMI sea-ice detection algorithm performance. The VIIRS data are processed by the National Oceanic and Atmospheric Administration (NOAA) and include many products related to snow and sea ice. Compared with the interactive multisensor snow and ice mapping system (IMS) daily Northern Hemisphere snow and ice analysis 4-km product, the accuracy of the VIIRS SIC EDR is 97.4% [19]. We used the VIIRS SIC EDR product from January 2018 to March 2018. The ice-age class of VIIRS SIC data are stratified into ice free, new/young ice, other ice and cloud; we employed ice free, new/young ice and other ice from the VIIRS SIC EDR.

3. Sea-ice Detection Algorithm

The GK-2A/AMI sea-ice detection algorithm aims to distinguish between the presence and absence of sea ice using optical sensor and has 3 steps (Figure 2), as follows:

1. Preprocessing of data and identification of potential sea ice areas;
2. Sea ice detection under clear skies; high confidence clear on GK-2A/AMI cloud mask;
3. Sea ice detection for the low-confidence cloudy, which is classified using the GK-2A/AMI cloud mask.

In step 1, we first applied to the land-sea mask provided by NMSC to distinguish the land and then in our algorithm, the visible channel data were mainly used as input data. For this reason, when SZA > 80°, the data were classified as nighttime data. After distinguishing land and nighttime, we classified sea ice candidate using long-term satellite-based sea-ice data. The long-term satellite-based sea-ice data were based on NSIDC's Northern Hemisphere EASE-Grid 2.0 Weekly snow cover and Sea-ice data from 1980 to 2014 for 35 years. Figure 3 shows the distribution ratio of sea ice among the EASE-Grid 2.0 Weekly snow cover and Sea-ice products from December to February from 1980 to 2014 in the study area of this study. The percentage of sea ice occurrence over 35 years is over 40% in the Okhotsk Sea and in the Bohai Sea (Figure 3). However, the distribution of sea ice occurrence in the Bohai Sea is extremely limited (Figure 3). The GK-2A/AMI sea-ice detection algorithm uses the long-term sea ice occurrence distribution ratio shown in Figure 3 to set the candidate sea area for sea ice. In the long-term sea ice occurrence distribution ratio, pixels in which sea ice existed even once were classified into candidate sea ice pixels. In case of sea ice pixel in long-term satellite-based sea-ice data, the GK-2A/AMI sea-ice detection algorithm classifies all nearby 5-by-5 pixels as sea ice candidates. The process of classifying the candidate sea ice regions is also used in other sea-ice detection algorithms. The global multisensor automated satellite-based snow and ice mapping system (GMASI) ice mapping algorithm utilizes latitude to identify potential ice areas [57].

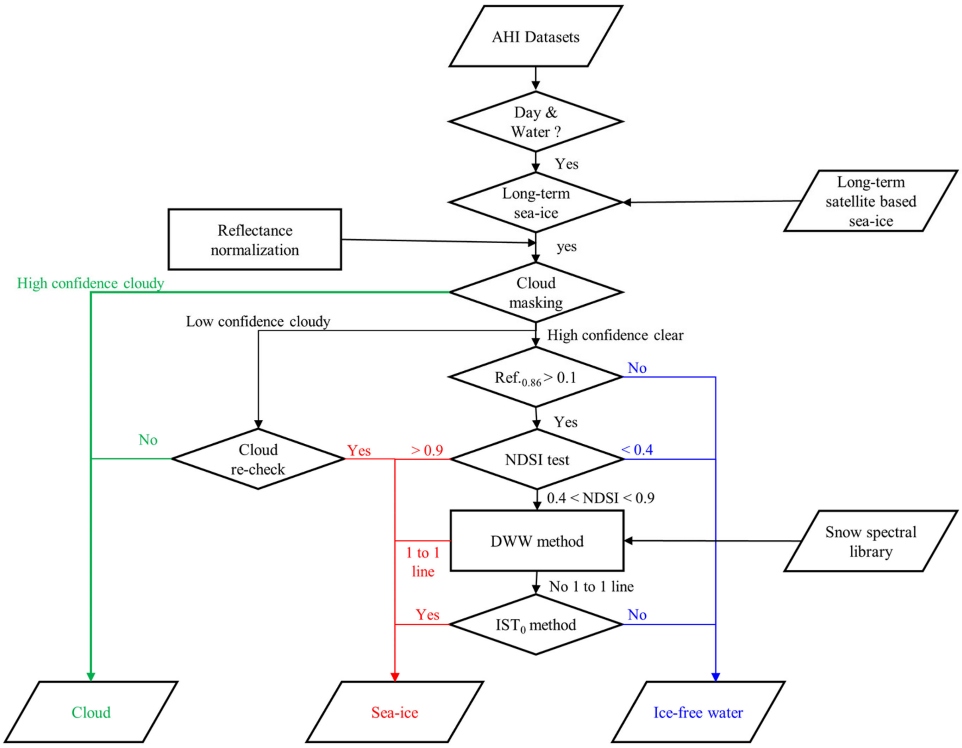

Figure 2. Flow chart showing GK-2A/AMI sea-ice detection algorithm; green line (cloud), red line (sea ice) and blue line (ice-free water).

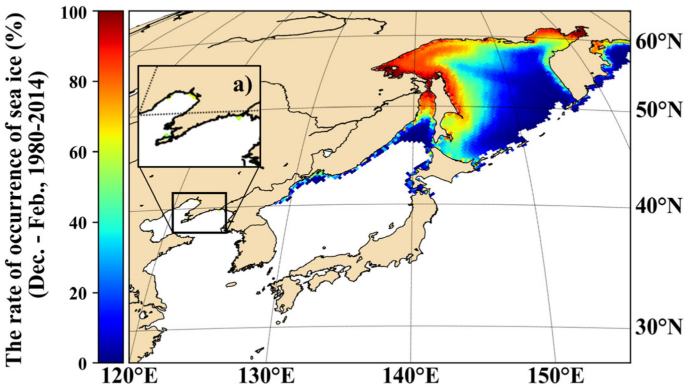

Figure 3. Statistical map of spatial occurrence rate of sea ice using long-term satellite-based sea-ice data (EASE-Grid 2.0 Weekly snow cover and Sea-ice Products of NSIDC) for research areas expanded from 1980 to 2014; (**a**) distribution of sea ice occurrence in the Bohai Sea.

Even when $SZA < 80°$, the visible channel data can be compromised. One limitation is the reflectance varies depending on SZA; if this dependency is ignored, errors in sea-ice detection can occur. Therefore, we applied to the following equation to minimize the variability according to SZA, by normalizing the reflectance at top-of-atmosphere (TOA) (Equation (2)). Reflectance normalization as performed by Temimi et al. (2011) [10] was also applied before performing sea-ice detection and reflectance normalization was executed not only during sea-ice detection, but also during snow cover detection [58].

$$R' = \frac{R}{\cos(SZA)}. \tag{2}$$

R in Equation (2) is the reflectance before normalization is applied, SZA is the solar zenith angle, and R' is the normalized reflectance.

Next, we applied the cloud mask to discriminate between cloudy and clear skies: "high-confidence cloudy" data were classified as cloudy and not used any further; "low-confidence cloudy" data were rechecked to determine the presence of sea ice; and "high-confidence clear" data were utilized for sea-ice detection. The reason for performing the recheck to the low-confidence cloudy is that the GK-2A/AMI cloud mask shows high accuracy in summer, but tends to over-detect the cloud in winter, and this feature is reflected in the sea-ice detection algorithm. The cloud recheck test based on static threshold method was performed to improve the area where the sea ice-in area was falsely detected as "low-confidence cloudy" on GK-2A/AMI cloud mask. The cloud recheck test includes $R_{1.61}$ test and test using the reflectance ratios of $R_{0.46}$ and $R_{1.61}$. Figure 4 shows the ratio of $R_{1.61}$ and reflectance ratio ($R_{0.46}$ and $R_{1.61}$) of Himawri-8/AHI in the area where GK-2A/AMI cloud mask is divided into low-confidence cloudy. The sea ice (Figure 4 red) and cloud (Figure 4 blue) on numeric distribution of Figure 4 are pixel information of the MOD29 data, which was reprojected to Himawri-8/AHI full disk, among the areas classified as low-confidence cloudy by the GK-2A/AMI cloud mask. The static threshold values were set based on the $R_{1.61}$ and reflectance ratio distribution in Figure 4. Figure 4a shows the distribution of $R_{1.61}$, and when $R_{1.61} > 0.2$, it is divided into clouds. Figure 4b shows the distribution of reflectance ratio of the sea ice candidate pixels, not classified by $R_{1.61}$. Based on this, the GK-2A/AMI sea-ice detection algorithm empirically reclassified sea ice when the reflectance ratio is less than 0.15.

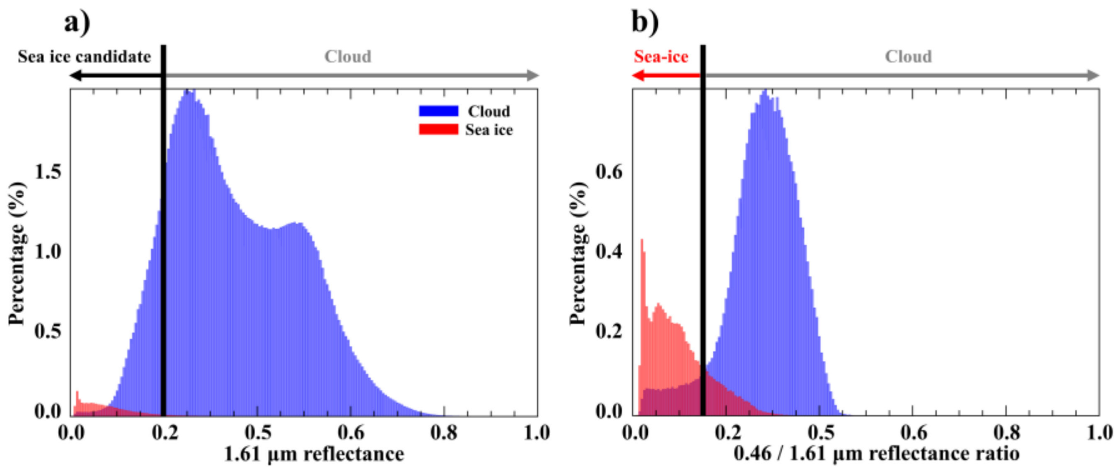

Figure 4. (**a**) distribution of $R_{1.61}$, and when $R_{1.61} > 0.2$, it is divided into clouds, (**b**) distribution of reflectance ratio of the sea ice candidate pixels, not classified by $R_{1.61}$. Targeting the "low-confidence cloudy" area, distribution on Himawari-8/AHI channel data ($R_{1.61}$ and ratio of $R_{0.46}$ and $R_{1.61}$) corresponding to MOD29 sea ice and cloud pixels, which are reprojected on Himawari-8/AHI full disk, Targeting the "low-confidence cloudy" area of the GK-2A/AMI cloud mask, it shows Himawari-8/AHI $R_{1.61}$ and ratio of $R_{0.46}$ and $R_{1.61}$, The cloud (blue) and sea ice (red) represent the MOD29 sea-ice data reprojected to Himawri-8/AHI. The black lines in figure are set empirically according to the value distribution of each index ($R_{1.61}$ and ratio of $R_{0.46}$ and $R_{1.61}$).

In step 2, we detected the presence or absence of sea ice in clear sky for pixels classified as "high-confidence clear" by the GK-2A/AMI cloud mask. The GK-2A/AMI sea-ice detection algorithm basically used MOD29 sea-ice pixels to build a sea-ice detection algorithm. For this progress, we performed reprojection of MOD29 sea ice/ice-free water pixels with Himawri-8/AHI full disk.

After selecting the sea ice candidate pixels, we applied to $R_{0.86}$ and NDSI based on the static threshold method for sea-ice detection. The MODIS and VIIRS were also used for static threshold method using $R_{0.86}$ and NDSI for sea-ice detection [4,19]. Although NDSI is widely used for sea-ice detection, NDSI shows NDSI value of the melting sea ice, including ice covered with snow, is lower than NDSI value of sea ice [59]. For this reason, we only detected pixels where we had high confidence that they were sea ice or ice-free water. The $R_{0.86}$ and NDSI thresholds were obtained using histograms from the MODIS sea ice extent and AHI reflectance data (Figure 5). For static thresholds, the focus was on distinguishing confidently between sea ice and ice-free water; for $R_{0.86}$, our threshold was 0.1 ($R_{0.86} > 0.1$ was sea ice and $R_{0.86} < 0.1$ was ice-free water; Figure 5a). Pixels that were not classified as ice-free water using $R_{0.86}$ were classified as ice-free water when NDSI < 0.4 (Figure 5b). In addition, pixels with NDSI ≥ 0.9 were classified as sea ice. Threshold value using NDSI was determined empirically using the distribution of sea ice and ice-free water as in $R_{0.86}$. Since the NDSI less than 0.4 sea ice is less than 1% of the total sea ice, it does not significantly affect the accuracy of the GK-2A/AMI sea-ice detection algorithm. Since ice-free water with an NDSI of 0.9 or higher is not even 0.1%, the GK-2A/AMI sea-ice detection algorithm is classified as sea ice when the NDSI is 0.9 or higher.

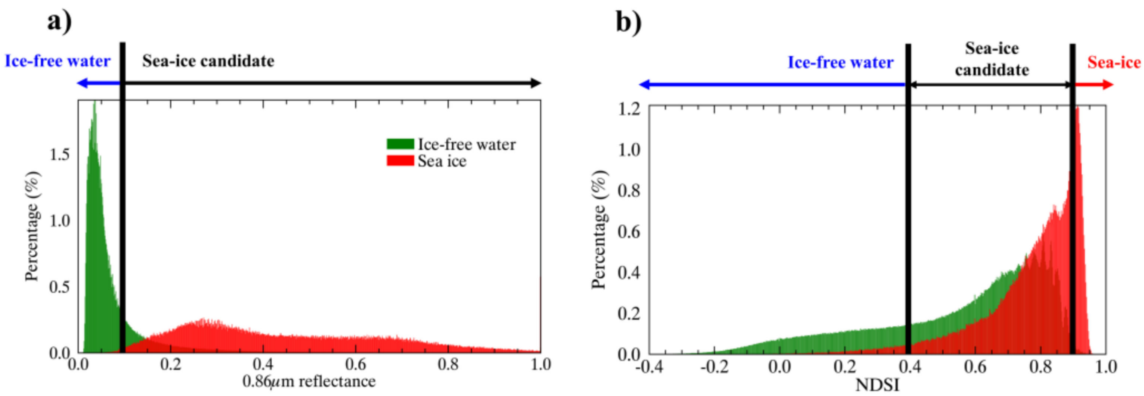

Figure 5. Distribution of (**a**) Himawari-8/AHI-based $R_{0.86}$ and (**b**) NDSI showing thresholds for sea ice/ice-free water in MODIS sea ice extent (MOD29) data. Black lines in figure are set empirically according to the value distribution of each index ($R_{0.86}$ and NDSI).

For the GK-2A/AMI sea-ice detection algorithm, dynamic threshold methods were applied to sea-ice candidates not classified as static threshold methods ($R_{0.86}$ and NDSI). This approach involved DWW and IST_0 tests. The DWW is a method for determining similarities between two data containing spectral features. In more detail, the similarities are determined by comparing the pattern of spectral reflectance change. Lee et al. (2017) [58] proposed and performed the DWW method to perform snow cover detection using MODIS satellite data. The snow cover data calculated through the DWW method was compared with MOD10 data and in-situ data. The overall accuracy (OA) compared to MOD10 data was 92.2%, and the OA accuracy compared to in-situ data is 93.6%. The OA is essentially out of all of the reference data what proportion were mapped correctly and refers to the ratio of correctly classified pixels to total number of pixels. Details of the OA calculation are given in Section 4.1. The GK-2A/AMI sea-ice detection algorithm utilized DWW to perform sea-ice detection considering the spectral characteristics of ice covered with snow among sea ice. In order to perform the DWW method, data for determining the similarity with reference are required. The GK-2A/AMI sea-ice detection algorithm built the snow spectral libraries (Figure 6) as reference data for the DWW method. To build the snow spectral libraries, spatial information of snow cover was obtained by performing reprojection of MOD10 data into the Himawari-8/AHI full disk observation area. The snow pixels among the MOD10 data on which the reprojection was performed, were identified spectral characteristics using channel data of Himawari-8/AHI. In other words, the snow spectral libraries were constructed with Himawari-8/AHI $R_{0.46}$, $R_{0.51}$, $R_{0.64}$, $R_{0.86}$, $R_{1.61}$, $BT_{11.2}$ and $BT_{3.8}$ corresponding to the MOD10 snow pixel where reprojection was performed. In this study, in addition to the snow spectral libraries, the data to determine the similarity is called a profile. In addition to the reflectance of the visible and near-infrared wavelength, we applied to the brightness temperature difference (*BTD*) consisting of $BT_{11.2}$ and $BT_{3.8}$. The *BTD* [$BT_{11.2}$–$BT_{3.8}$] (BTD_1) is used to detect cloud [18,60]. To setup the snow spectral libraries and profile, we normalized BTD_1 to match the value range of channel reflectance (Equation (3)).

$$Nor.\ BTD_1 = \frac{(BTD_{1,\ Max} - BTD_1)}{(BTD_{1,\ Max} - BTD_{1,\ Min})}. \tag{3}$$

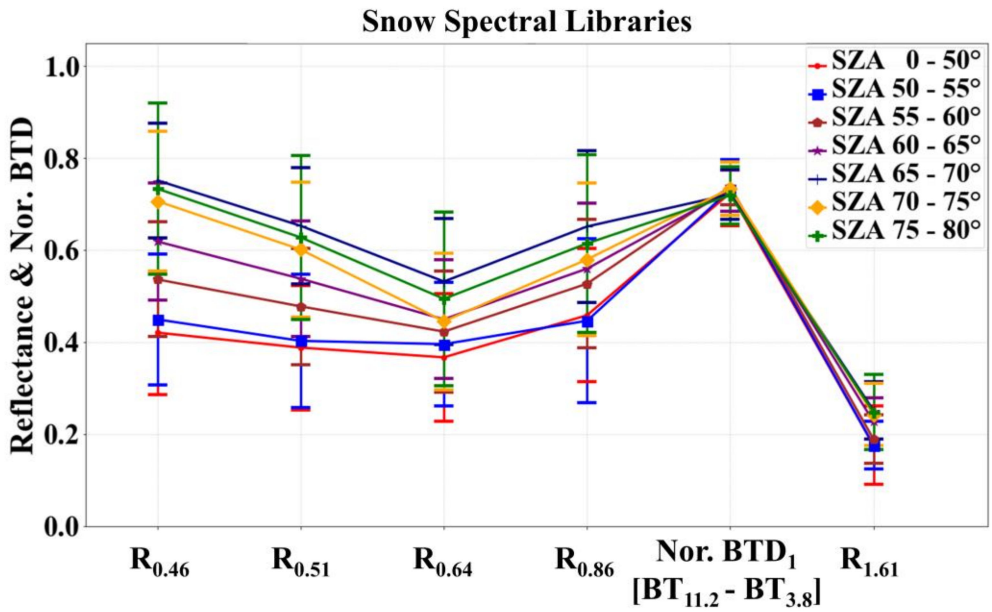

Figure 6. Snow spectral libraries using the reflectivity and brightness temperature of Himawri-8/AHI and snowfall data reprojected to Himawri-8/AHI full disk, 7 Snow spectral libraries according to SZA, X-axis of snow spectral libraries is $R_{0.46}$, $R_{0.51}$, $R_{0.64}$, $R_{0.86}$, BTD_1, $R_{1.61}$ data, the Y-axis is the average value and standard deviation of the reflectance and BTD corresponding to the X-axis.

As a result of analyzing BTD_1 of MOD10 snow cover pixels (11,531,002) obtained from GK-2A/AMI sea-ice detection algorithm, Maximum value of BTD_1 is 80.0 and Minimum value is −30.0. In Equation (3), the corresponding values were applied to $\mathrm{BTD}_{1,\ \mathrm{Max.}}$ and $\mathrm{BTD}_{1,\ \mathrm{Min}}$. The reason for adding BTD_1 to existing channel data are to reduce the possibility of false detection of cloud as sea ice. In detail, the GK-2A/AMI sea-ice detection algorithm uses the GK-2A/AMI cloud mask to distinguish the cloud area. However, if a real cloud region that is not classified as a cloud exists in high-confidence clear of the GK-2A/AMI cloud mask, there is a possibility of false detection of the real cloud region as sea ice. In the GK-2A/AMI sea-ice detection algorithm, we built snow spectral libraries considering the variability of sea-ice reflectance according to SZA. The snow spectral libraries were generated by dividing SZA into 7 ranges (0–50°, 50–55°, 55–60°, 60–65°, 65–70°, 70–75°, 75–80°).

Figure 6 shows the snow spectral libraries for each SZA range. When we performed DWW, we utilized a snow spectral library in the same SZA range as for the sea-ice candidate pixel.

The snow spectral libraries according to SZA showed a unique pattern. In addition, $R_{0.46}$, $R_{0.51}$, $R_{0.64}$, $R_{0.86}$ show that the reflectance variability was large. Prior to performing the sea-ice detection through DWW method, a snow spectral library according to the SZA of the sea-ice candidate pixel was selected, and a profile reflecting the spectral characteristics of the sea-ice candidate pixel was set. In the DWW, the difference between the 6 index values of the snow spectral library and the 6 index values of the profile was calculated. Next, the cumulative smallest cost was calculated using the difference in values between each element of the snow spectral library and profile. This created a cumulative smallest cost of 6-by-6 (Figure 7a-2,b-2). The subsequent process progress from the start point ([6,6] on Figure 7a-2,b-2; $R_{1.61}$, the 6th index of the snow spectral library and profile) to cumulative smallest cost with the smallest value among the surrounding cumulative smallest costs. Finally, its processes were executed to the last point ([1,1] on Figure 7a-2, b-2; $R_{0.46}$ 1st index of the snow spectral library and profile). The traces of progress from [6,6] to [1,1] in Figure 7a-2,b-2 are called warping path. When the warping path that is the final result of the DWW method is 1:1 line, it means that the profile is similar to the snow spectral library. Figure 7a-1 shows the pixel snow spectral library and profile with a 1:1-line of warping path and Figure 7a-2 shows the cumulative smallest cost and warping path of 6-by-6. If the warping path that is the final result of the DWW method is not 1:1 line, it means that the profile is not similar to the snow spectral library. Figure 7b-1 shows a pixel snow spectral library and profile with not resulting in a warping path not 1:1 line and Figure 7b-2 shows a cumulative smallest cost and warping path of 6-by-6. The GK-2A/AMI sea-ice detection algorithm executed to classify as sea ice as the warping path resulting in a warping path 1:1 line. If the warping path is not 1:1, the next sea-ice detection method was performed.

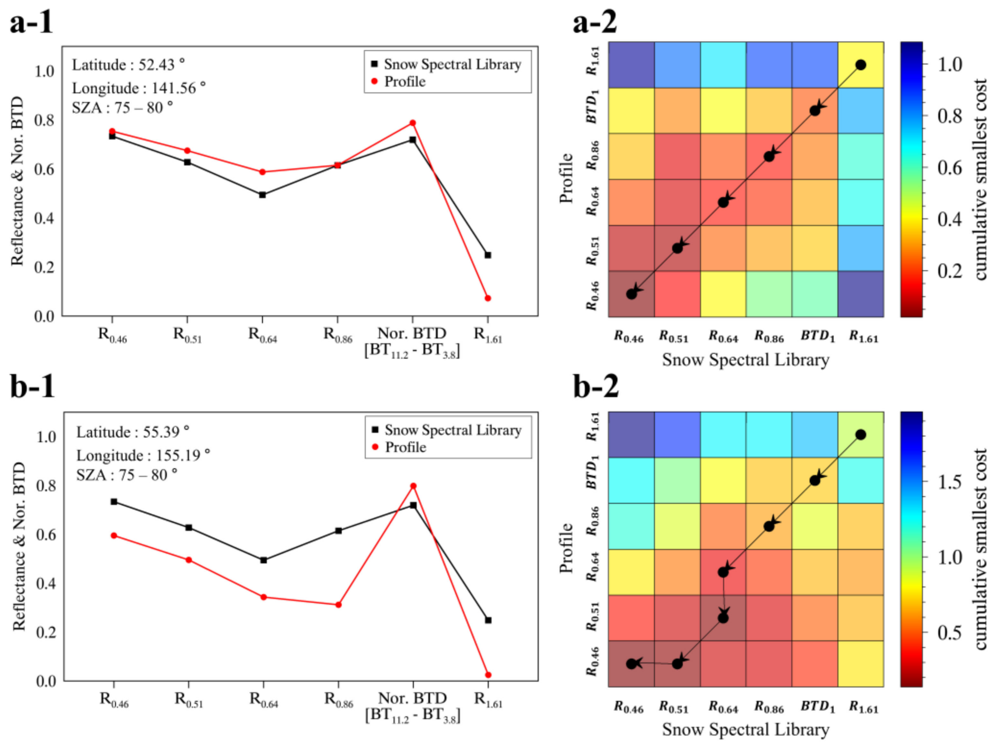

Figure 7. DWW method applied to GK-2A/AMI sea-ice detection algorithm, (**a-1**,**b-1**); snow spectral library (*X*-axis: $R_{0.46}$, $R_{0.51}$, $R_{0.64}$, $R_{0.86}$, Nor. BTD$_1$, $R_{1.61}$, *Y*-axis: reflectance and Nor. BTD$_1$ value) selected according to the SZA of the sea-ice candidate pixel and the profile (*X*-axis: $R_{0.46}$, $R_{0.51}$, $R_{0.64}$, $R_{0.86}$, Nor. BTD$_1$, $R_{1.61}$, *Y*-axis: Reflectance and Nor. BTD$_1$ value) of the sea-ice candidate pixel, (**a-2**,**b-2**); DWW result of the snow spectral library selected according to the SZA of the sea-ice candidate pixel and the profile of the sea-ice candidate pixel (e.g., cumulative smallest cost, warping path).

After using DWW for detection of snow-covered ice, we used the IST_0 method to detect bare **ice** (i.e., not snow-covered). This method is constructed based on the interrelationship between *IST*, $BT_{11.2}$ and *BTD* [$BTD_2 = BT_{11.2}–BT_{12.4}$, in this method] and in this study, the corresponding sea-ice detection test was called IST_0 method. Jin et al. (2017) [61] performed and evaluated sea-ice detection using MODIS data with the IST_0 method. The sea-ice data calculated through the IST_0 method was compared with MOD29 data. The accuracy compared to MOD29 data was over 99% OA. Figure 8 shows the relationship between $BT_{11.2}$ and BTD_2 according to IST. The red line in Figure 8 shows the relationship between BTD_2 and $BT_{11.2}$ when IST was 271.0 K and the red dotted line below shows the relationship between BTD_2 and $BT_{11.2}$ when IST was 261.0 K and 251.0 K. Based on the results in Figure 8, it can be determined that $BT_{11.2}$ and BTD_2 are linear according to IST. When the IST reaches 271.0 K, since sea ice has generated, the GK-2A/AMI sea-ice detection algorithm derived the first-order linear equation by utilizing the relationship between $BT_{11.2}$ and BTD_2 at IST = 271.0 K (Equation (4)). In the GK-2A/AMI sea-ice detection algorithm, when IST becomes 271.0 K, the result of Equation (4) according to BTD_2 is defined as IST_0. Using this, if the $BT_{11.2}$ is lower than result value of Equation (4) according to BTD_2, the corresponding pixel was classified as sea ice ($BT_{11.2} < IST_0$ (e.g., result value of Equation (4) according to BTD_2) → sea ice).

$$IST_0 = -2.056 \times BTD_2 + 273.1. \tag{4}$$

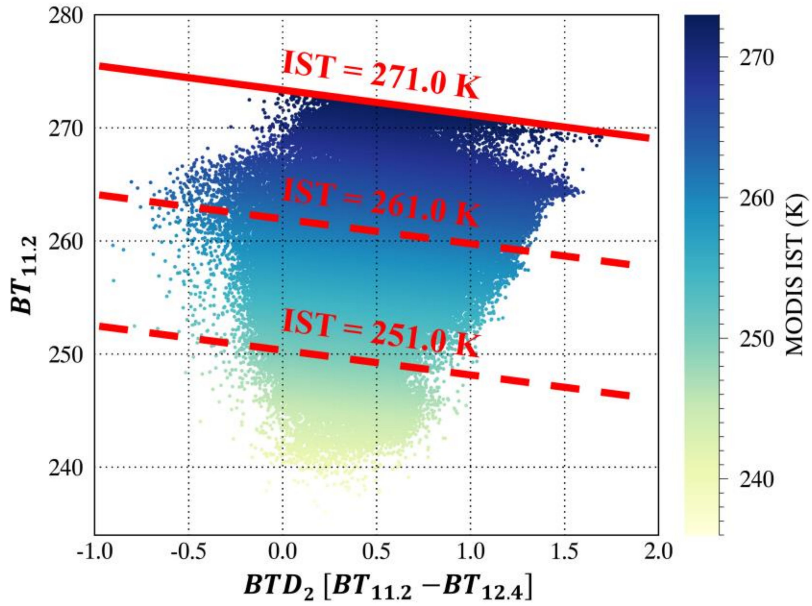

Figure 8. Distribution of relationship between $BT_{11.2}$ and BTD_2 [$=BT_{11.2}–BT_{12.4}$] using MODIS IST, Red line indicates that $BT_{11.2}$ and BTD_2 are linear in the 271.0 K environment where the sea water freezes. Red dotted line shows linear relationship. Dotted lines below indicate that $BT_{11.2}$ and BTD_2 are linear when IST = 261.0 K and IST = 251.0 K.

In step 3, we rechecked the cloud mask results ("cloud recheck"). The sea-ice detection algorithm uses the GK-2A/AMI cloud mask provided by NMSC to distinguish cloud regions, but some "low-confidence cloudy" on the GK-2A/AMI cloud mask include areas where actual sea ice were detected as cloud pixel. Therefore, we conducted a cloud recheck to detect sea ice among the "low-confidence cloudy" pixels. We used static thresholds for $R_{1.61}$ and reflectance ratio calculated with $R_{0.46}$ and $R_{1.61}$. Figure 9 shows a Himawri-8/AHI RGB image (Figure 9a) and the sea-ice data obtained in GK-2A/AMI sea-ice detection algorithm, before (Figure 9b) and after (Figure 9c) the cloud recheck. Figure 9b shows the result of GK-2A/AMI sea-ice detection algorithm before cloud recheck test was applied. In the sea-ice image before the cloud recheck test was applied, sea ice only distributed along the coastline of the Okhotsk Sea, an area where the GK-2A/AMI cloud mask was classified as "high-confidence clear". Compared with the Himawari-8/AHI RGB image (Figure 9a), the GK-2A/AMI cloud mask detected the sea-ice regions widely distributed in the Okhotsk Sea into "low-confidence cloudy". In this case, the GK-2A/AMI sea-ice detection algorithm lost the opportunity to detect sea ice. Figure 9c is a GK-2A/AMI sea-ice image to which the cloud recheck test is applied and the GK-2A/AMI sea-ice detection algorithm detects the sea-ice area distributed in the Okhotsk Sea.

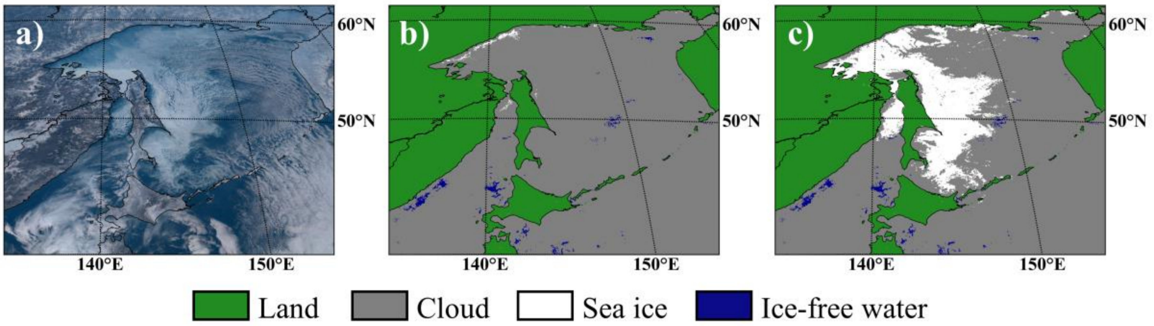

Figure 9. (**a**) Himawari-8/AHI RGB image (WSDbank); (**b**) sea-ice data map image using GK-2A/AMI sea-ice detection algorithm without cloud recheck; and (**c**) after cloud recheck at 0330 UTC on 3 November 2018.

4. Validation Results of GK-2A/AMI Sea-Ice Detection Algorithm

4.1. Comparison/Validation Method

We utilized both quantitative and qualitative comparison/validation methods to evaluate the accuracy of GK-2A/AMI sea-ice detection algorithm. For comparing with S-NPP/VIIRS SIC, we calculated the following metrics: OA (consistency), Inconsistency, POD and FAR. These metrics are frequently used for validation of detection studies [58,61–63]. The OA (consistency) is calculated using a contingency table (Table 1; hit, false, miss, correct rejection) along with Equation (5). The inconsistency is calculated using Equation (6) with values from Table 1 (e.g., false and miss were numerator and hit, false, miss, correct rejection were denominator). POD is calculated using a contingency table (Table 1) along with Equation (7); it uses all available validation data. FAR is calculated using Equation (8) with values from Table 1. As FAR approaches 0%, the evaluated data become worse. S-NPP/VIIRS SIC cannot be regarded as sea-ice truth data because satellite data-based sea-ice data are not in situ-data. Accordingly, the GK-2A/AMI sea-ice detection algorithm utilized Consistency, Inconsistency as comparing S-NPP/VIIRS SIC.

$$OA,\ Consistency = \left(\frac{a+d}{a+b+c+d}\right) \times 100. \tag{5}$$

$$Inconsistency = \left(\frac{b+c}{a+b+c+d}\right) \times 100. \tag{6}$$

$$POD = \left(\frac{a}{a+c}\right) \times 100. \tag{7}$$

$$FAR = \left(\frac{b}{a+b}\right) \times 100. \tag{8}$$

we compared GK-2A/AMI sea-ice detection results with S-NPP/VIIRS SIC EDR, and additionally, Himawari-8/AHI RGB images (WSDbank), to determine whether GK-2A/AMI sea-ice detection algorithm accurately detected areas of sea ice. Sea ice has characteristics similar to those of clouds, which indicates that clouds contribute to the largest errors in sea-ice detection. To accurately determine the presence or absence of clouds and sea ice, we utilized the fact that the mobility of clouds over time is faster than sea ice. Using image observation time to compare GK-2A/AMI sea-ice detection algorithm's sea-ice data and the S-NPP/VIIRS SIC and Himawari-8/AHI RGB images before and after, we grasped the movement of clouds over time and performed qualitative validation using them.

Table 1. Contingency table for comparing data from GK-2A/AMI sea-ice detection algorithm with S-NPP/VIIRS SIC EDR/sea-ice ROI data. Values (a), (b), (c) and (d) are used in Equations (5)–(8).

GK-2A/AMI Sea-Ice Detection Algorithm	Comparison/Validation Data	
	Sea Ice	**Ice-Free Water**
Sea ice	Hit (a)	False (b)
Ice-free water	Miss (c)	Correct rejection (d)

We executed indirect comparison of the sea-ice data generated by GK-2A/AMI sea-ice detection algorithm using S-NPP/VIIRS SIC EDR, but there is a limit to the fact that the sea-ice data of the algorithm is accurate by simply comparing it with other satellite sea-ice data. The ideal validation method is to validate the sea-ice data of this algorithm by using in situ data. However, it is difficult to obtain a large amount of observation data, since the area where sea ice exists is that humans cannot easily access and observe. In this reason, we constructed the sea-ice ROI data through photo-interpretation method based on Himawari-8/AHI RGB images. The photo-interpretation method is one of the validation methods for detection research using satellite data, and is used for various detection research (e.g., vehicles, seagrass and colonized hard bottom detection and land cover classification using satellite data) [64–66]. In the GK-2A/AMI sea-ice detection algorithm, the POD, FAR and OA were used for comparison with sea-ice ROI data.

4.2. Comparison with S-NPP/VIIRS Sea-Ice Characterization Environmental Data Record

To compare our sea-ice detection algorithm data with S-NPP/VIIRS SIC EDR, we limited time difference between Himawri-8/AHI and S-NPP/VIIRS. The time difference threshold was within 5 min. In addition, we performed reprojection of the S-NPP/VIIRS SIC EDR pixels to the Himawari-8/AHI using the latitude and longitude data of S-NPP/VIIRS and Himawari-8/AHI. We set new/young ice and other ice as sea ice and set ice free as ice-free water among flag information of S-NPP/VIIRS SIC EDR. In addition, we excluded cloudy pixels from the S-NPP/VIIRS SIC data; we aim to evaluate accuracy of the presence or absence of sea ice, then performed a 1:1-pixel comparison with our sea-ice output data for January 2018 to March 2018, using a total of 68 images. Figure 10 shows the consistency, inconsistency and sea-ice rate on valid pixels of S-NPP/VIIRS SIC EDR and sea-ice data according to the study period. The sea-ice rate on valid pixel is the ratio of sea-ice pixels among all pixels in the S-NPP/VIIRS SIC EDR image. It also provides quantitative results for our comparison of the GK-2A/AMI sea-ice detection algorithm against the S-NPP/VIIRS SIC EDR, with Consistency = 99.0% and Inconsistency = 0.9% for January 2018 to March 2018. We analyzed 3 cases in detail, using the S-NPP/VIIRS SIC EDR and Himawari-8/AHI RGB images. We divided the 3 Cases and performed further analysis. We performed additional analysis based on the consistency, inconsistency and sea-ice rate on valid pixels on S-NPP/VIIRS SIC scene in Figure 10. In the S-NPP/VIIRS SIC Scene, the ratio of sea ice was classified based on 20%. This is because sea ice is limited except in polar regions and certain regions (Okhotsk Sea and Bohai Sea). The Case 1 was performed on a scene with low sea-ice rate in S-NPP/VIIRS SIC scene and low consistency and high inconsistency with S-NPP/VIIRS SIC (16 January 2018, 00:26 UTC). Case 2 was targeted for scenes with high sea-rate in S-NPP/VIIRS SIC scene and low consistency and high inconsistency with S-NPP/VIIRS SIC (24 January 2018, 01:14 UTC). Case 3 was a scene that shows a high consistency and low inconsistency with S-NPP/VIIRS SIC.

Case 1: Low consistency/High inconsistency, sea-ice rate among S-NPP/VIIRS SIC scene < 20%:

The corresponding pixels are from 2 scenes: 00:26 UTC on 16 January 2018 and 04:50 UTC on 23 January 2018. Qualitative analyses relative to Himawari-8/AHI RGB images confirm that the false detection of these two scenes in the GK-2A/AMI sea-ice detection algorithm is cloudy for Himawari-8/AHI RGB images, but that the S-NPP/VIIRS data are misdiagnosed as sea ice. Figure 11 shows images of the S-NPP/VIIRS SIC EDR (Figure 11a), GK-2A/AMI sea-ice data (Figure 11b) and Himawari-8/AHI RGB (Figure 11d) at 00:30 UTC on 16 January 2018. For our qualitative analysis using

Himawari-8/AHI RGB imagery, we used scenes from ±2 h (Figure 11c,e) and ±1 day (Figure 11f,g). Comparing the S-NPP/VIIRS SIC EDR (Figure 11a) with our sea-ice data (Figure 11b), It was shown that S-NPP/VIIRS SIC does not classify the actual sea-ice zone as sea ice; S-NPP/VIIRS could not detect this area (red circle). Based on the Himawari-8/AHI RGB image, it appears that the sea ice was distributed along the coastline; S-NPP/VIIRS SIC EDR could not detect this result for that same area (Figure 11 red circle).

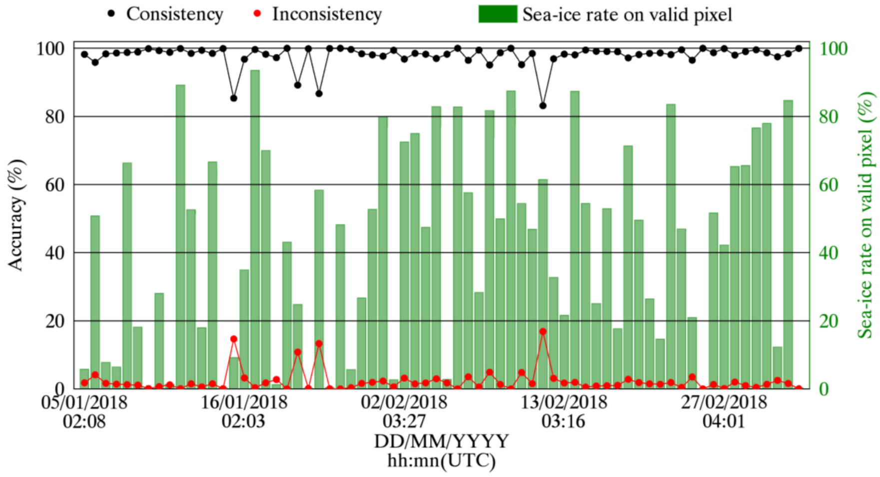

Figure 10. Time–series of consistency/inconsistency in the sea-ice data using GK-2A/AMI sea-ice detection algorithm than S-NPP/VIIRS SIC EDR data from January to March 2018, "sea-ice rate on valid pixel" means the distribution ratio of sea ice among all pixels of the S-NPP/VIIRS SIC Scene.

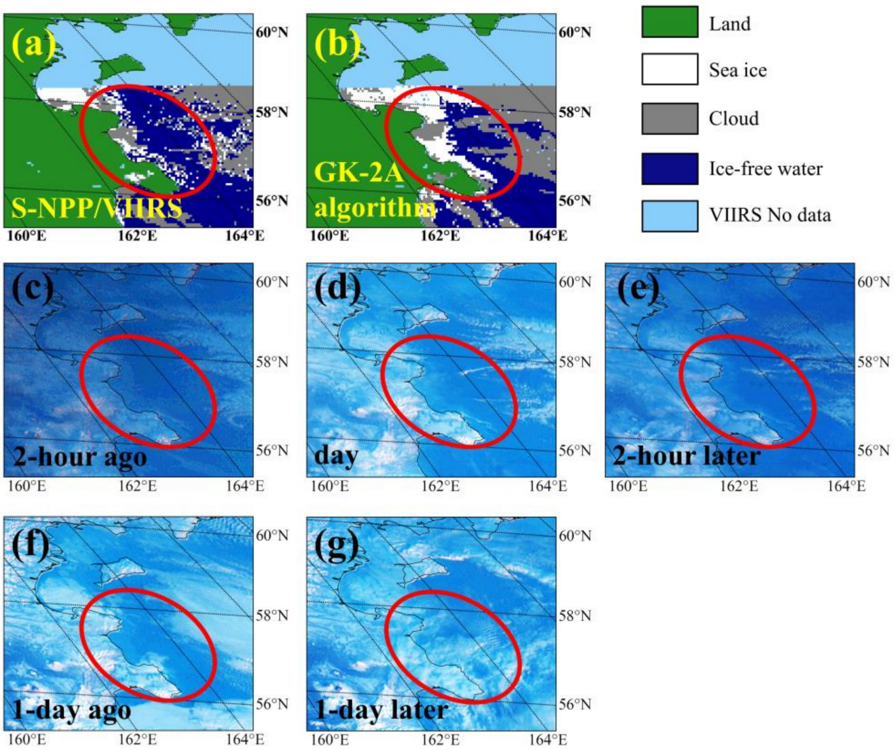

Figure 11. (**a**) S-NPP/VIIRS SIC EDR data at 00:26 UTC, 16 January 2018, (**b**) sea-ice data using GK-2A/AMI sea-ice detection algorithm at 00:30 UTC, 16 January 2018, (**c**) Himawari-8/AHI RGB image at 22:30 UTC, 15 January 2018, (**d**) Himawari-8/AHI RGB image at 00:30 UTC, 16 January 2018, (**e**) Himawari-8/AHI RGB image at 02:30 UTC, 15 January 2018, (**f**) Himawari-8/AHI RGB image at 00:30 UTC, 15 January 2018 and (**g**) Himawari-8/AHI RGB image at 00:30 UTC, 17 January 2018.

Case 2: Low consistency/High inconsistency, sea-ice rate among S-NPP/VIIRS SIC scene > 20%:

The corresponding pixels are from 3 scenes in 03:50 UTC on 10 January 2018, 02:51 UTC on 24 January 2018 and 02:34 UTC on 5 February 2018. Based upon the Himawari-8/AHI RGB images, the sea-ice area not detected by GK-2A/AMI sea-ice detection algorithm is a mix of clouds and ice-free water; S-NPP/VIIRS falsely detected sea ice. Figure 12 shows images of the Himawari-8/AHI RGB image (Figure 12c–g), S-NPP/VIIRS SIC EDR (Figure 12a) and GK-2A/AMI sea-ice data (Figure 12b) at 03:50 UTC on 10 January 2018. Comparing the S-NPP/VIIRS SIC EDR (Figure 12a) with GK-2A/AMI sea-ice data (Figure 12b), GK-2A/AMI sea-ice detection algorithm showed far fewer sea-ice pixels to detect falsely than S-NPP/VIIRS SIC (Figure 12 red circle). As a result of confirming Himawari-8/AHI RGB images (Figure 12c–g), it was determined that there was no sea ice in the red circle. For this region, neither S-NPP/VIIRS SIC EDR nor GK-2A/AMI sea-ice detection algorithm could detect the sea ice and S-NPP/VIIRS SIC EDR showed a greater tendency to overestimate the sea-ice extent.

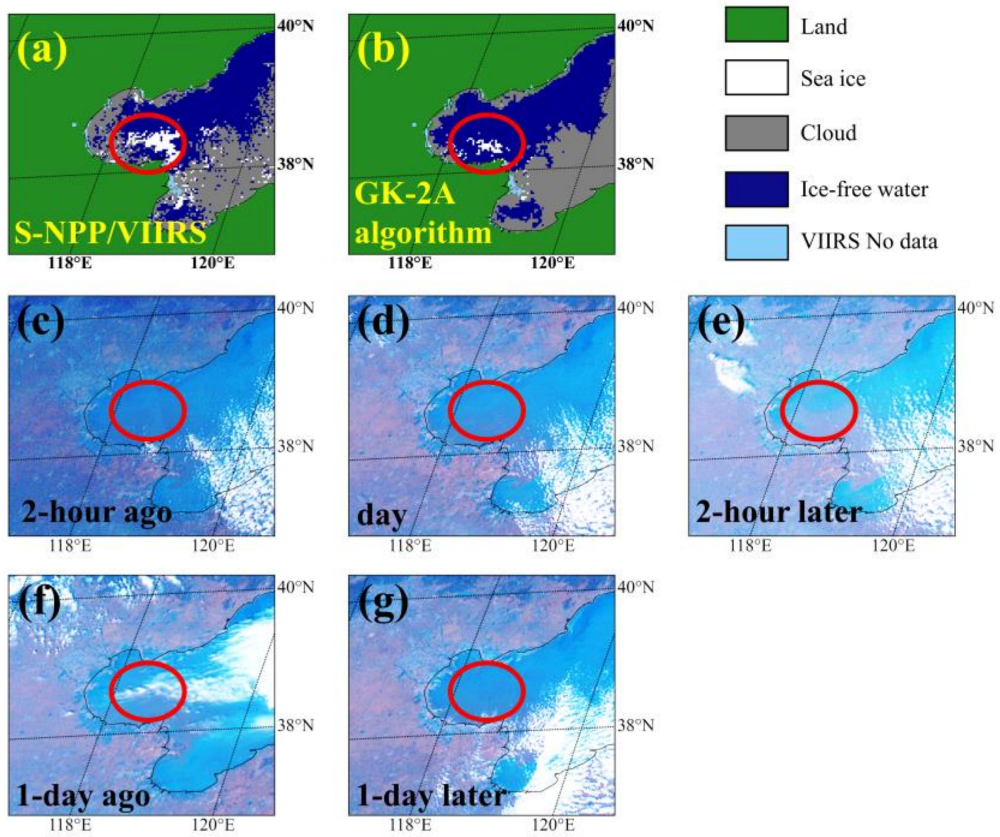

Figure 12. (**a**) S-NPP/VIIRS SIC EDR data at 03:53 UTC, 10 January 2018, (**b**) sea-ice data using GK-2A/AMI detection algorithm at 03:50 UTC, 10 January 2018, (**c**) Himawari-8/AHI RGB images at 02:00 UTC, 10 January 2018, (**d**) Himawari-8/AHI RGB images at 03:50 UTC, 10 January 2018, (**e**) Himawari-8/AHI RGB images at 06:00 UTC, 10 January 2018, (**f**) Himawari-8/AHI RGB images at 03:50 UTC 9 January 2018 and (**g**) Himawari-8/AHI RGB images at 03:50 UTC, 11 January 2018.

Case 3: High consistency/Low inconsistency:

The corresponding pixels are in the case except the previous 2 cases. Figure 13 shows the images from 03:30 UTC on 11 March 2018. Using AHI RGB imagery, for the same time increments as in Cases 1 and 2, we determined that there was sea ice in the corresponding area. Comparing the S-NPP/VIIRS SIC EDR (Figure 13a) with GK-2A/AMI sea-ice detection sea-ice data (Figure 13b), GK-2A/AMI sea-ice detection algorithm has fewer false positive pixels than the S-NPP/VIIRS SIC. S-NPP/VIIRS SIC EDR detected sea ice as clouds in some areas. However, GK-2A/AMI sea-ice detection algorithm detects the sea-ice region well.

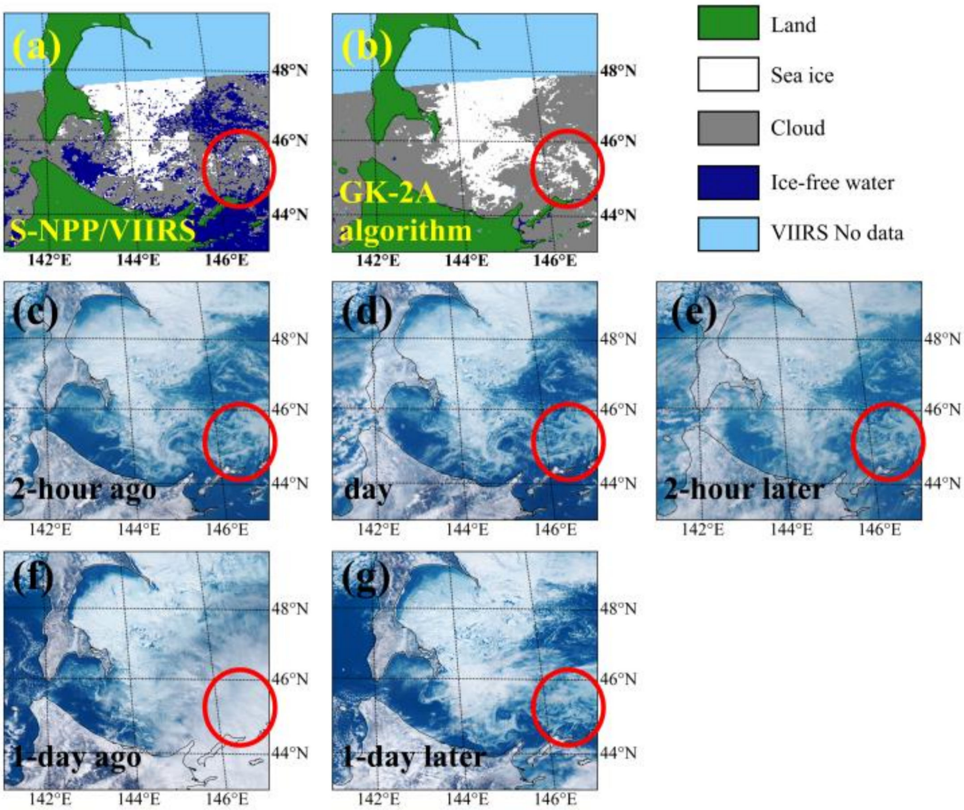

Figure 13. (**a**) S-NPP/VIIRS SIC EDR data at 03:28 UTC, 11 March 2018, (**b**) sea-ice data using GK-2A/AMI sea-ice detection algorithm at 03:30 UTC, 11 March 2018, (**c**) Himawari-8/AHI RGB images at 01:30 UTC, 11 March 2018, (**d**) Himawari-8/AHI RGB images at 03:30 UTC, March 2018, (**e**) Himawari-8/AHI RGB images at 05:30 UTC, 11 March 2018, (**f**) Himawari-8/AHI RGB images at 03:30 UTC, 10 March 2018 and (**g**) Himawari-8/AHI RGB images at 03:30 UTC, 12 March 2018.

4.3. Performance with Sea-Ice ROI Data

In the previous section, we performed indirect comparison of the sea-ice data generated by GK-2A/AMI sea-ice detection algorithm using S-NPP/VIIRS SIC EDR and Himawari-8/AHI RGB images. The sea-ice ROI data were built by manually performing photo-interpretation method in area sea-ice and ice-free water using the Himawari-8/AHI RGB images. In the classification, all the scene was secured and analyzed for every 10 min of the day that the specific scene was included and the Himawari-8/AHI RGB images of the day before and the next day was also secured and used. As a result of photo-interpretation method, 10 scenes, 182,133 validation points were secured from January to March 2018. The validation using the sea-ice ROI data were performed 1:1 comparison of the S-NPP/VIIRS SIC EDR data and the data calculated by the GK-2A/AMI sea-ice detection algorithm on this research with sea-ice ROI data were performed and comparison was made between sea ice and ice-free water pixels. The sea-ice ROI data confirmed and secured reliable sea ice and ice-free water areas and also compared S-NPP/VIIRS SIC EDR data with the sea-ice data calculated using the GK-2A/AMI sea-ice detection algorithm for accuracy comparison. The validation date was randomly selected from the scenes where S-NPP/VIIRS SIC EDR data existed from January to March 2018 and a total of 10 scenes were tested. Table 2 shows the result of validating the sea-ice data of the GK-2A/AMI sea-ice detection algorithm and the S-NPP/VIIRS SIC data using sea-ice ROI data. Both POD and OA have higher accuracy than 96% in both sea-ice data obtained through GK-2A/AMI sea-ice detection algorithm and S-NPP/VIIRS SIC. In the case of the FAR, all of sea-ice ROI data showed a value of 0.0% because the number of reliable ice-free water pixels in the clear sky was very small.

Table 2. Comparison result of GK-2A/AMI sea-ice detection algorithm, S-NPP/VIIRS SIC using sea-ice ROI data for 10 scenes.

YYYYMMDD.hhmn (S-NPP/VIIRS Time)	GK-2A/AMI Sea-Ice Detection Algorithm		S-NPP/VIIRS SIC EDR	
	POD/FAR (%)	OA (%)	POD/FAR (%)	OA (%)
20180112.0140 (0142)	98.35/0.00	98.35	61.48/0.00	61.48
20180116.0200 (0203)	98.01/0.00	98.11	97.85/0.00	97.96
20180116.0350 (0345)	98.81/0.00	98.82	95.51/0.00	95.53
20180203.0310 (0309)	94.70/0.00	94.70	99.23/0.00	99.23
20180203.0450 (0451)	98.73/0.00	98.73	97.96/0.00	97.96
20180204.0250 (0246)	94.15/0.00	95.70	98.52/0.00	98.90
20180204.0250 (0252)	95.97/0.00	95.97	99.87/0.00	99.87
20180216.0400 (0400)	99.70/0.00	99.89	98.18/0.00	99.34
20180220.0250 (0250)	96.14/0.00	96.14	98.37/0.00	98.34
20180311.0330 (0333)	93.85/0.00	94.06	88.48/0.00	88.87
Total	96.54/0.00	97.23	96.00/0.00	96.81

5. Discussion and Conclusions

We developed GK-2A/AMI sea-ice detection algorithm considering the reflectance variability of sea ice using Himawari-8/AHI data with similar characteristics to GK-2A/AMI. Sea-ice detection using existing optical satellites mainly uses NDSI and IST based on the static threshold method [4–6]. Optical satellites also include geostationary satellites GOES-R/ABI. Since sea-ice detection based on the static threshold method lacks the part that considers the spectrum variability of sea ice, it is possible to occur the error when detecting melting sea ice, which have variabilities of spectral characteristics. For the GK-2A/AMI sea-ice detection algorithm, dynamic threshold methods (e.g., DWW and IST_0 method) were applied considering the variability of sea ice. The DWW is a method for determining similarity, which is determined by comparing the pattern of reflectance change that changes depending on the wavelength of data. Lee et al. (2017) [58] employed the DWW method to perform snow detection and GK-2A/AMI sea-ice detection algorithm applied DWW method to sea-ice detection and added BTD considering the spectral characteristics of clouds to reflectance according to the existing wavelength. By adding BTD_1 to spectral libraries and profiles, the GK-2A/AMI sea-ice detection algorithm improves the false detection errors by sea ice for areas where the GK-2A/AMI cloud mask does not classify the actual cloud area as a cloud. Its method was used to perform sea-ice detection considering the spectral characteristics of sea ice covered with snow. The IST_0 method performed using a simple dynamic threshold that does not require IST coefficients or IST calculation. The IST coefficient required to calculate IST is calculated through linear regression using various variables, and this process was a complicated process. This process is complicated because sea-ice detection [4–6,19] using existing IST requires calculating the IST coefficient for each satellite. Because the IST0 method has a purpose of detecting the presence or absence of sea ice, the dynamic threshold method of $BT_{11.2}$ was employed without using IST. In the case of snow and sea-ice detection, it is most important to distinguish it from clouds and other institutions (e.g., NOAA, JMA) are also performing snow detection and snow detection after classifying the clouds using the cloud mask of each satellite [4,5,67,68]. Since sea-ice detection algorithm utilizes cloud mask to eliminate cloud, the accuracy of cloud mask has a great influence on sea-ice detection algorithm. To improve this part, GK-2A/AMI sea-ice detection algorithm performed a cloud recheck test on the cloud area among the cloud masks to classify the actual sea-ice area classified as cloud as sea-ice. Indirect validation using S-NPP/VIIRS SIC EDR data and 68 scenes showed a high agreement rate of 99.0% for consistency and 0.9% for inconsistency. As a result of comparison with the sea-ice ROI data, the Oa of GK-2A/AMI sea-ice detection algorithm is 97.2%, S-NPP/VIIRS SIC is 96.81%. In the area where cloud and ice-free water are mixed, S-NPP/VIIRS SIC

EDR falsely detects the cloud in the area as sea ice, but GK-2A/AMI sea-ice detection algorithm shows an improvement that is not classified as sea ice.

The GK-2A/AMI sea-ice detection algorithm utilized geostationary satellite data, where channel data were calculated at 10-min intervals. The sea-ice data calculated by this algorithm are also calculated at 10-min intervals, so real-time monitoring of sea-ice is possible for specific areas. daily sea-ice data, such as MODIS [16], is classified as sea-ice if sea-ice exists even once for 24 h due to the limitation of the polar-orbit satellite. However, since this algorithm produces up to 144 sea-ice data over a 24-h period, it is possible to improve the potential sea-ice false positive rate when producing daily sea-ice data. Since high-accuracy, integrated daily sea-ice data can be used as input data to the weather forecast model, it can contribute significantly to the weather forecast model compared to the existing sea-ice data. Sea-ice data based on the GK-2A/AMI sea-ice detection algorithm expects to help not only for climate research, but also for sea transportation and tourism.

In the future, the GK-2A/AMI sea-ice detection algorithm will be optimized using GK-2A/AMI satellite data during the winter period of 2019–2020 NORTHERN Hemisphere. When using GK-2A/AMI satellite data, $R_{1.38}$ are planned to be additionally utilized and the accuracy of the sea-ice data are expected to be further improved through $R_{1.38}$ data. The $R_{1.38}$ is a channel mainly used for detecting thin clouds and should be considered when performing optimization of the GK-2A/AMI sea-ice detection algorithm in the future.

The GK-2A/AMI sea-ice detection algorithm was evaluated using S-NPP/VIIRS SIC data, which is satellite data-based sea-ice data and sea ice ROI data based on photo-interpretation. Like other sea-ice detection algorithms using satellite data [4–8,18], the GK-2A/AMI sea-ice detection algorithm performed comparisons using satellite data-based sea-ice data in the absence of sea ice truth data. The GK-2A/AMI sea-ice detection algorithm is significant in that it compares sea-ice data with other satellites and additionally performs accuracy evaluation using sea ice ROI data. Currently, sea ice in situ data mainly provide buoy data. Sea ice buoy data includes the International arctic buoy program (IABP) and the International program for Antarctic buoys (IPAB) Antarctic drifting buoy data. However, since the Buoy-based sea-ice data are extremely limited in space, there are limitations to using them immediately. The others sea ice in situ data are collected through field campaigns such as Multidisciplinary drifting observatory for the study of arctic climate (MOSAiC). The MOSAiC is the first year-round expedition into the central arctic exploring the arctic climate system (e.g., September 2019~September 2020). High-spatial-resolution optical satellite-based sea-ice data includes ice information among European space agency (ESA) Sentinel-2/multispectral instrument (MSI) Level-2 data [69]. Since the Sentinel-2/MSI Level-2 data have a spatial resolution of 10–20 m, it includes sea ice information requiring high-resolution sea-ice data such as ice drift, sea ice edges; High-spatial-resolution satellite-based sea-ice data also includes microwave-based SAR images. In the future, the GK-2A/AMI sea-ice detection algorithm will evaluate the verifiability using sea ice in situ data and the high-spatial-resolution satellite-based sea-ice data.

Author Contributions: Conceptualization, D.J. (Donghyun Jin), K.-S.L. and K.-S.H.; methodology, D.J. (Donghyun Jin) and K.-S.L.; validation, D.J. (Donghyun Jin) and D.J. (Daeseong Jung); formal analysis, D.J. (Donghyun Jin), S.C. and N.-H.S.; investigation D.J. (Donghyun Jin), K.-S.L. and S.S.; writing—original draft preparation, D.J. (Donghyun Jin); writing—review and editing, D.J. (Donghyun Jin), M.S., S.C. and N.-H.S.; visualization, D.J. (Donghyun Jin), K.-S.L. and M.S.; supervision, K.-S.H.; project administration, S.-R.C. and J.K. All authors have read and agreed to the published version of the manuscript.

Funding: Authors (Donghyun Jin, Sungwon Choi, Noh-Hun Seong, Deseong Jung, Suyoung Sim) were supported by the BK21 plus Project of the Graduate School of Earth Environmental Hazard System.

Acknowledgments: This work was supported by "Development of the GK2A meteorological algorithms" project, funded by ETRI, which is a subproject of "Development of geostationary Meteorological Satellite Ground Segment" program funded by NMSC/KMA. We thank KMA's NMSC for providing Himawari-8/AHI Dataset and Cloud Mask, and this work was a part of the project titled 'Korea-Arctic Ocean Observing System(K-AOOS), KOPRI, 20160245)', funded by the MOF, Korea. The authors are indebted to anonymous reviewers for their useful comments that improved the manuscript.

Conflicts of Interest: The authors declare no conflicts of interest.

References

1. Ledley, T.S. A coupled energy balance climate-sea ice model: Impact of sea ice and leads on climate. *J. Geophys. Res. Atmos.* **1988**, *93*, 15919–15932. [CrossRef]
2. Cavalieri, D.J.; Parkinson, C.L. Arctic sea ice variability and trends, 1979–2010. *Cryosphere* **2012**, *5*, 881. [CrossRef]
3. Meier, W.N.; Markus, T.; Comiso, J.; Ivanoff, A.; Miller, J. *AMSR2 Sea Ice Algorithm Theoretical Basis Document*; NASA Goddard Space Flight Center: Greenbelt, MD, USA, 2017.
4. Hall, D.K.; Riggs, G.A.; Salomonson, V.V.; Barton, J.S.; Casey, K.; Chien, J.Y.L.; DiGirolamo, N.E.; Klein, A.G.; Powell, H.W.; Tait, A.B. *Algorithm Theoretical Basis Document (ATBD) for the MODIS Snow and Sea Ice-Mapping Algorithms*; NASA Goddard Space Flight Center: Greenbelt, MD, USA, 2001; Volume 45.
5. Baker, N. *Joint Polar Satellite System (JPSS) VIIRS Sea Ice Characterization Algorithm Theoretical Basis Document (ATBD)*; NASA Goddard Space Flight Center Green belt; NASA Goddard Space Flight Center: Greenbelt, MD, USA, 2011.
6. Liu, Y.; Key, J.R. *Algorithm Theoretical Basis Document (ATBD); Ice Surface Temperature, Ice Concentration and Ice Cover*; NOAA Nesdis Center for Satellite Applications and Research: Silver Spring, MD, USA, 2019.
7. Ioka, Y.; Yogo, Y.; Tanikawa, T.; Hosaka, M.; Ishida, H.; Aoki, T. Algorithm Theoretical Basis for the Himawari-8,-9/AHI Cryosphere Product Part 2: Sea Ice Distribution. *Meteorol. Satell. Cent. Tech. Note* **2019**, *64*, 13–21.
8. Ludwig, V.; Spreen, G.; Haas, C.; Istomina, L.; Kauker, F.; Murashkin, D. The 2018 North Greenland polynya observed by a newly introduced merged optical and passive microwave sea-ice concentration dataset. *Cryosphere* **2019**, *13*, 2051–2073. [CrossRef]
9. Zakhvatkina, N.; Smirnov, V.; Bychkova, I. Satellite sar data-based sea ice classification: An overview. *Geosciences* **2019**, *9*, 152. [CrossRef]
10. Temimi, M.; Romanov, P.; Ghedira, H.; Khanbilvardi, R.; Smith, K. Sea-ice monitoring over the Caspian Sea using geostationary satellite data. *Int. J. Remote Sens.* **2011**, *32*, 1575–1593. [CrossRef]
11. Gerland, S.; Barber, D.; Meier, W.; Mundy, C.J.; Holland, M.; Kern, S.; Li, Z.; Michel, C.; Perovich, D.K.; Tamura, T. Essential gaps and uncertainties in the understanding of the roles and functions of Arctic sea ice. *Environ. Res. Lett.* **2019**, *14*, 043002. [CrossRef]
12. Seong, N.H.; Jung, D.; Kim, J.; Han, K.S. Evaluation of NDVI Estimation Considering Atmospheric and BRDF Correction through Himawari-8/AHI. *Asia Pac. J. Atmos. Sci.* **2020**, *5*, 1–10. [CrossRef]
13. Lee, K.S.; Lee, C.S.; Seo, M.; Choi, S.; Seong, N.H.; Jin, D.; Yeom, J.M.; Han, K.S. Improvements of 6S Look-Up-Table Based Surface Reflectance Employing Minimum Curvature Surface Method. *Asia Pac. J. Atmos. Sci.* **2020**, *3*, 1–14. [CrossRef]
14. Choi, Y.Y.; Suh, M.S. Development of Himawari-8/Advanced Himawari Imager (AHI) land surface temperature retrieval algorithm. *Remote Sens.* **2018**, *10*, 2013. [CrossRef]
15. Lee, S.J.; Ahn, M.H.; Chung, S.R. Atmospheric profile retrieval algorithm for next generation geostationary satellite of Korea and its application to the advanced Himawari Imager. *Remote Sens.* **2017**, *9*, 1294. [CrossRef]
16. Lee, S.H.; Kim, B.Y.; Lee, K.T.; Zo, I.S.; Jung, H.S.; Rim, S.H. Retrieval of reflected shortwave radiation at the top of the atmosphere using Himawari-8/AHI data. *Remote Sens.* **2018**, *10*, 213. [CrossRef]
17. Oh, S.M.; Borde, R.; Carranza, M.; Shin, I.C. Development and Intercomparison Study of an Atmospheric Motion Vector Retrieval Algorithm for GEO-KOMPSAT-2A. *Remote Sens.* **2019**, *11*, 2054. [CrossRef]
18. Imai, T.; Yoshida, R. Algorithm theoretical basis for Himawari-8 cloud mask product. *Meteorol. Satell. Cent. Tech. Note* **2016**, *61*, 1–17.
19. Key, J.R.; Mahoney, R.; Liu, Y.; Romanov, P.; Tschudi, M.; Appel, I.; Maslanik, J.; Baldwin, D.; Wang, X.; Meade, P. Snow and ice products from Suomi NPP VIIRS. *J. Geophys. Res. Atmos.* **2013**, *118*. [CrossRef]
20. Ning, L.; Xie, F.; Gu, W.; Xu, Y.; Huang, S.; Yuan, S.; Cui, W.; Levy, J. Using remote sensing to estimate sea ice thickness in the Bohai Sea, China based on ice type. *Int. J. Remote Sens.* **2009**, *30*, 4539–4552. [CrossRef]
21. Key, J.R.; Wang, X.; Stoeve, J.C.; Fowler, C. Estimating the cloudy-sky albedo of sea ice and snow from space. *J. Geophys. Res. Atmos.* **2001**, *106*, 12489–12497. [CrossRef]
22. Mundy, C.J.; Barber, D.G.; Michel, C. Variability of snow and ice thermal, physical and optical properties pertinent to sea ice algae biomass during spring. *J. Mar. Syst.* **2005**, *58*, 107–120. [CrossRef]
23. Nazari, R.; Khanbilvardi, R. Application of dynamic threshold in sea and lake ice mapping and monitoring. *Int. J. Hydrol. Sci. Technol.* **2011**, *1*, 37–46. [CrossRef]

24. Warren, S.G. Optical properties of snow. *Rev. Geophys.* **1982**, *20*, 67. [CrossRef]
25. Cline, D.; Rost, A.; Painter, T.; Bovitz, C. *Algorithm Theoretical Basis Document (ATBD)*; Snow Cover; NOAA Nesdis Center for Satellite Applications and Research: Silver Spring, MD, USA, 2010.
26. Xin, Q.; Woodcock, C.E.; Liu, J.; Tan, B.; Melloh, R.A.; Davis, R.E. View angle effects on MODIS snow mapping in forests. *Remote Sens. Environ.* **2012**, *118*, 50–59. [CrossRef]
27. Key, J.R.; Collins, J.B.; Fowler, C.; Stone, R.S. High-latitude surface temperature estimates from thermal satellite data. *Remote Sens. Environ.* **1997**, *61*, 302–309. [CrossRef]
28. Yan, Y.; Huang, K.; Shao, D.; Xu, Y.; Gu, W. Monitoring the Characteristics of the Bohai Sea Ice Using High-Resolution Geostationary Ocean Color Imager (GOCI) Data. *Sustainability* **2019**, *11*, 777. [CrossRef]
29. Miao, X.; Xie, H.; Ackley, S.F.; Perovich, D.K.; Ke, C. Object-based detection of Arctic sea ice and melt ponds using high spatial resolution aerial photographs. *Cold Reg. Sci. Technol.* **2015**, *119*, 211–222. [CrossRef]
30. Zhang, N.; Ma, Y.; Zhang, Q. Prediction of sea ice evolution in Liaodong Bay based on a back-propagation neural network model. *Cold Reg. Sci. Technol.* **2018**, *145*, 65–75. [CrossRef]
31. Honda, M.; Yamazaki, K.; Nakamura, H.; Takeuchi, K. Dynamic and thermodynamic characteristics of atmospheric response to anomalous sea-ice extent in the Sea of Okhotsk. *J. Clim.* **1999**, *12*, 3347–3358. [CrossRef]
32. Minervin, I.G.; Romanyuk, V.A.E.; Pishchal'nik, V.M.; Truskov, P.A.E.; Pokrashenko, S.A. Zoning the ice cover of the Sea of Okhotsk and the Sea of Japan. *Her. Russ. Acad. Sci.* **2015**, *85*, 132–139. [CrossRef]
33. Wakabayashi, H.; Mori, Y.; Nakamura, K. Sea ice detection in the sea of Okhotsk using PALSAR and MODIS data. *IEEE J. Sel. Top. Appl. Earth Obs. Remote Sens.* **2013**, *6*, 1516–1523. [CrossRef]
34. Nihashi, S.; Kurtz, N.T.; Markus, T.; Ohshima, K.I.; Tateyama, K.; Toyota, T. Estimation of sea-ice thickness and volume in the Sea of Okhotsk based on ICESat data. *Ann. Glaciol.* **2018**, *59*, 101–111. [CrossRef]
35. Toyota, T.; Baba, K.; Hashiya, E.; Ohshima, K.I. In-situ ice and meteorological observations in the southern Sea of Khotsk in 2001 winter: Ice structure, snow on ice, surface temperature, and optical environments. *Polar Meteorol. Glaciol.* **2002**, *16*, 116–132.
36. Shi, W.; Wang, M. Sea ice properties in the Bohai Sea measured by MODIS-Aqua: 1. Satellite algorithm development. *J. Mar. Syst.* **2012**, *95*, 32–40. [CrossRef]
37. Su, H.; Wang, Y.; Yang, J. Monitoring the spatiotemporal evolution of sea ice in the Bohai Sea in the 2009–2010 winter combining MODIS and meteorological data. *Estuaries Coasts* **2012**, *35*, 281–291. [CrossRef]
38. Karvonen, J.; Shi, L.; Cheng, B.; Similä, M.; Mäkynen, M.; Vihma, T. Bohai Sea ice parameter estimation based on thermodynamic ice model and Earth observation data. *Remote Sens.* **2017**, *9*, 234. [CrossRef]
39. Yan, Y.; Shao, D.; Gu, W.; Liu, C.; Li, Q.; Chao, J.; Tao, J.; Xu, Y. Multidecadal anomalies of Bohai Sea ice cover and potential climate driving factors during 1988–2015. *Environ. Res. Lett.* **2017**, *12*, 094014. [CrossRef]
40. Yan, Y.; Uotila, P.; Huang, K.; Gu, W. Variability of sea ice area in the Bohai Sea from 1958 to 2015. *Sci. Total Environ.* **2020**, *709*, 136164. [CrossRef]
41. Su, H.; Ji, B.; Wang, Y. Sea Ice Extent Detection in the Bohai Sea Using Sentinel-3 OLCI Data. *Remote Sens.* **2019**, *11*, 2436. [CrossRef]
42. NMSC: GK-2A AMI Algorithm Theoretical Basis Document. Available online: http://nmsc.kma.go.kr/homepage/html/base/cmm/selectPage.do?page=static.edu.atbdGk2a (accessed on 15 April 2019).
43. Murata, K.T.; Pavarangkoon, P.; Higuchi, A.; Toyoshima, K.; Yamamoto, K.; Muranaga, K.; Nagaya, Y.; Izumikawa, Y.; Kimura, E.; Mizuhara, T. A web-based real-time and full-resolution data visualization for Himawari-8 satellite sensed images. *Earth Sci. Inform.* **2018**, *11*, 217–237. [CrossRef]
44. Riggs, G.A.; Hall, D.K.; Salomonson, V.V. *MODIS Sea Ice Products User Guide to Collection 5*; NASA Goddard Space Flight Center: Greenbelt, MD, USA, 2006; Volume 49.
45. Hall, D.K.; Key, J.R.; Casey, K.A.; Riggs, G.A.; Cavalieri, D.J. Sea ice surface temperature product from the Moderate Resolution Imaging Spectroradiometer (MODIS). *IEEE Trans. Geosci. Remote Sens.* **2004**, *42*, 1076–1087. [CrossRef]
46. Shuman, C.A.; Hall, D.K.; DiGirolamo, N.E.; Mefford, T.K.; Schnaubelt, M.J. Comparison of near-surface air temperatures and MODIS ice-surface temperatures at Summit, Greenland (2008–13). *J. Appl. Meteorol.* **2014**, *53*, 2171–2180. [CrossRef]
47. Scambos, T.A.; Haran, T.M.; Massom, R. Validation of AVHRR and MODIS ice surface temperature products using in situ radiometers. *Ann. Glaciol.* **2006**, *44*, 345–351. [CrossRef]
48. Rösel, A.; Kaleschke, L.; Birnbaum, G. Melt ponds on Arctic sea ice determined from MODIS satellite data using an artificial neural network. *Cryosphere* **2012**, *6*, 431–446. [CrossRef]

49. Mäkynen, M.; Karvonen, J. MODIS sea ice thickness and open water–sea ice charts over the Barents and Kara Seas for development and validation of sea ice products from microwave sensor data. *Remote Sens.* **2017**, *9*, 1324. [CrossRef]
50. Hall, D.K.; Riggs, G.A. Accuracy assessment of the MODIS snow products. *Hydrol. Process.* **2007**, *21*, 1534–1547. [CrossRef]
51. Huang, X.; Liang, T.; Zhang, X.; Guo, Z. Validation of MODIS snow cover products using Landsat and ground measurements during the 2001–2005 snow seasons over northern Xinjiang, China. *Int. J. Remote Sens.* **2011**, *32*, 133–152. [CrossRef]
52. Hall, D.K.; Foster, J.L.; Verbyla, D.L.; Klein, A.G.; Benson, C.S. Assessment of snow-cover mapping accuracy in a variety of vegetation-cover densities in central Alaska. *Remote Sens. Environ.* **1998**, *66*, 129–137. [CrossRef]
53. Wang, X.; Xie, H.; Liang, T. Evaluation of MODIS snow cover and cloud mask and its application in Northern Xinjiang, China. *Remote Sens. Environ.* **2008**, *112*, 1497–1513. [CrossRef]
54. Maskey, S.; Uhlenbrook, S.; Ojha, S. An analysis of snow cover changes in the Himalayan region using MODIS snow products and in-situ temperature data. *Clim. Chang.* **2011**, *108*, 391. [CrossRef]
55. Rikiishi, K.; Hashiya, E.; Imai, M. Linear trends of the length of snow-cover season in the Northern Hemisphere as observed by the satellites in the period 1972–2000. *Ann. Glaciol.* **2004**, *38*, 229–237. [CrossRef]
56. Estilow, T.W.; Young, A.H.; Robinson, D.A. A long-term Northern Hemisphere snow cover extent data record for climate studies and monitoring. *Earth Syst. Sci. Data* **2015**, *7*, 137. [CrossRef]
57. Romanov, P. Global multisensor automated satellite-based snow and ice mapping system (GMASI) for cryosphere monitoring. *Remote Sens. Environ.* **2017**, *196*, 42–55. [CrossRef]
58. Lee, K.S.; Jin, D.; Yeom, J.M.; Seo, M.; Choi, S.; Kim, J.J.; Han, K.S. New Approach for Snow Cover Detection through Spectral Pattern Recognition with MODIS Data. *J. Sensors* **2017**. [CrossRef]
59. Gignac, C.; Bernier, M.; Chokmani, K.; Poulin, J. IceMap250—Automatic 250 m sea ice extent mapping using MODIS data. *Remote Sens.* **2017**, *9*, 70. [CrossRef]
60. Thoss, A. Algorithm Theoretical Basis Document for SAF NWC/PPS "Cloud Mask"(CM-PGE01 v. 3.0, patch 1) (No. 2.3, p. 48). SAF/NWC/CDOP/SMHI-PPS/SCI/ATBD/1. 2010. Available online: http://www.nwcsaf.org/AemetWebContents/ScientificDocumentation/Documentation/PPS/v2014/NWC-CDOP2-PPS-SMHI-SCI-ATBD-1_v1_0.pdf (accessed on 13 July 2020).
61. Jin, D.; Lee, K.S.; Choi, S.; Seo, M.; Lee, D.; Kwon, C.; Kim, H.; Lee, E.K.; Han, K.S. Determination of dynamic threshold for sea-ice detection through relationship between 11 μm brightness temperature and 11–12 μm brightness temperature difference. *Korean J. Remote Sens.* **2017**, *33*, 243–248.
62. Siljamo, N.; Hyvärinen, O. New Geostationary Satellite–Based Snow-Cover Algorithm. *J. Appl. Meteorol.* **2011**, *50*, 1275–1290. [CrossRef]
63. Chaouch, N.; Temimi, M.; Romanov, P.; Cabrera, R.; McKillop, G.; Khanbilvardi, R. An automated algorithm for river ice monitoring over the Susquehanna River using the MODIS data. *Hydrol. Process.* **2014**, *28*, 62–73. [CrossRef]
64. Gerhardinger, A.; Ehrlich, D.; Pesaresi, M. Vehicles detection from very high resolution satellite imagery. *Int. Arch. Photogramm. Remote Sens.* **2015**, *36*, W24.
65. Baumstark, R.; Duffey, R.; Pu, R. Mapping seagrass and colonized hard bottom in Springs Coast, Florida using WorldView-2 satellite imagery. *Estuar. Coast. Shelf Sci.* **2016**, *181*, 83–92. [CrossRef]
66. Inglada, J.; Vincent, A.; Arias, M.; Tardy, B.; Morin, D.; Rodes, I. Operational high resolution land cover map production at the country scale using satellite image time series. *Remote Sens.* **2017**, *9*, 95. [CrossRef]
67. Hall, D.K.; Riggs, G.A.; Salomonson, V.V.; DiGirolamo, N.E.; Bayr, K.J. MODIS snow-cover products. *Remote Sens. Environ.* **2002**, *83*, 181–194. [CrossRef]
68. Hutchison, K.D.; Iisager, B.D.; Mahoney, R.L. Enhanced snow and ice identification with the VIIRS cloud mask algorithm. *Remote Sens. Lett.* **2013**, *4*, 929–936. [CrossRef]
69. Louis, J.; Devignot, O.; Pessiot, L. S2 MPC–L2A Product Definition Document. Ref. S2-PDGS-MPC-L2A-PDD-V14, 2(4.6). 2018. Available online: https://sentinel.esa.int/documents/247904/685211/S2+L2A+Product+Definition+Document/2c0f6d5f-60b5-48de-bc0d-e0f45ca06304 (accessed on 11 July 2020).